Mass Transfer in the Laminar Radial Wall Jet

M. T. SCHOLTZ and OLEV TRASS

University of Toronto, Toronto, Ontario, Canada

Data are reported for mass transfer from a flat plate under the influence of a laminar, radial wall jet initiated by a free jet of water.

Present theory has been extended to mass transfer for the case of the above wall jet. An exact solution of the mass transport equation was obtained as well as an approximate solution of the integral mass balance equation, using assumed forms of the velocity and concentration profiles.

Point mass transfer data were obtained by measuring the thickness decrease of coatings of acetanilide and benzoic acid. In the Reynolds number range of 1,000 to 3,000 (based on the nozzle diameter) data were in good agreement with theory. Boundary-layer separation and the formation of a toroidal vortex were observed at lower Reynolds numbers. Dye streak photographs of these vortices were obtained and correlated with mass transfer data in this region.

The term radial wall jet applies to that boundary layer which develops when a submerged round, free jet of fluid impinges on a flat surface and spreads radially over that surface. This type of wall jet is shown in Figure 1. Ideally the boundary-layer thickness vanishes at the origin which can be considered to be a point momentum source in the radial direction. A second type of wall jet is the plane, two-dimensional wall jet.

All theoretical work which has been done on the wall jet has been based on the assumption that the boundary layer is self-preserving in form. However, there has been no experimental evidence to confirm this. Glauert (*1*) made an analysis of the equations of motion for both the axisymmetrical and two-dimensional wall jets and obtained a solution of the boundary-layer equations on the basis of self-preservation. Schwartz and Caswell (*2*) extended Glauert's exact solution for the two-dimensional case to heat transfer with constant physical properties, neglecting viscous dissipation. These authors also examined the plane wall jet by the momentum integral technique. It would appear from the literature than no experimental work has been done on the laminar wall jet, either plane or radial.

It is the aim of this work to extend Glauert's momentum analysis of the three-dimensional wall jet to mass transfer and to compare the theory with experimental data.

THEORY

Exact Solution of the Boundary-Layer Equations

The boundary-layer equations for axisymmetrical flow follow:

Momentum equation

$$u\frac{\partial u}{\partial x} + v\frac{\partial u}{\partial y} = \nu\frac{\partial^2 u}{\partial y^2} \tag{1}$$

Tabulated data are available in reference 6; the run numbers in the figures refer to these data.

Continuity

$$\frac{\partial (xu)}{\partial x} + \frac{\partial (xv)}{\partial y} = 0 \tag{2}$$

Mass conservation

$$u\frac{\partial c}{\partial x} + v\frac{\partial c}{\partial y} = D\frac{\partial^2 c}{\partial y^2} \tag{3}$$

The boundary conditions to be satisfied are

$$\begin{aligned} y = 0, \quad & u = v = 0, \quad c = c_o \\ y = \infty, \quad & u = 0, \qquad c = c_\infty \end{aligned} \tag{4}$$

for low rates of transfer as in this case. At high dissolution rates the normal velocity at the wall could not be assumed zero. An exact solution of Equation (1) was obtained by Glauert on the assumption that the boundary layer is self-preserving, that is, a similar solution exists. The solution was expressed in terms of F, the exterior flux of momentum flux, which is given by Equation (5) and which was shown by Glauert to be a constant and independent of radial position:

$$F = \int_o^\infty xu \int_o^\infty xu^2\, dy \cdot dy = \text{constant} \tag{5}$$

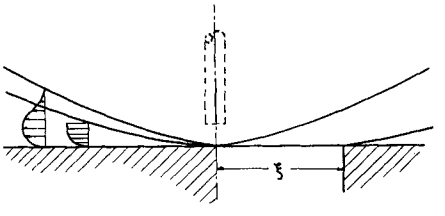

Fig. 1. The radial wall jet showing the concentration and momentum boundary layers with and without an uncoated starting length, right and left, respectively.

TABLE 1. DIMENSIONLESS CONCENTRATION GRADIENTS AT THE WALL

N_{Sc}	$[-g'(0)]$	N_{Sc}	$[-g'(0)]$
1.0	0.3333	500	2.962
2.0	0.4445	1,000	3.733
5.0	0.6241	1,500	4.274
10.0	0.7953	2,000	4.700
15.0	0.9138	3,000	5.385
100.0	1.731	4,000	5.921

The solution of (3) is obtained in a similar manner with a dimensionless concentration parameter

$$\frac{c - c_\infty}{c_o - c_\infty} = g(\eta) \tag{6}$$

where η is the similarity transform used by Glauert. It is zero at the wall and becomes infinite as $y \to \infty$. The solution for the dimensionless gradient at the wall is

$$[-g'(0)] = \frac{\Gamma(N_{Sc} + 1/3)}{\Gamma(N_{Sc})\Gamma(1/3)} \tag{7}$$

where Γ is the gamma function. Values of $[-g'(0)]$ computed from this equation are given in Table 1 for Schmidt numbers from 1 to 4,000. To allow for the fact that in the practical case of the wall jet the boundary conditions are not satisfied at $x = 0$, Glauert (3) introduced a length parameter l. For the plane wall jet l is the location of the virtual origin. The significance of l in the radial case however, is not as simple as this.

With the rate of mass transfer at the wall given by

$$N_o = k(c_o - c_\infty) = -D\left.\frac{dc}{dy}\right|_o \tag{8}$$

the solution in terms of the transfer coefficient, k, can be expressed as

$$k = 1.433\, D\left[\frac{F}{\nu^3}\right]^{1/4}[-g'(0)]\, x^{-5/4}\left[1 + \left(\frac{l}{x}\right)^3\right]^{-3/4} \tag{9}$$

Approximate Solution of the Integral Mass Balance Equation

The integral equations follow below:

Momentum: Multiply (1) by x and integrate with respect to y from zero to infinity

$$\frac{d}{dx}\int_o^\infty xu^2\, dy = \frac{-\tau_o x}{\rho} = -x\nu\left.\frac{du}{dy}\right|_o \tag{10}$$

Exterior flux of momentum flux (Glauert)

$$F = \int_o^\infty xu \int_o^\infty xu^2\, dy \cdot dy \tag{11}$$

Mass: Multiply (3) by x and integrate from zero to infinity

$$\frac{d}{dx}\int_o^\infty xu\,(c - c_o)\, dy = \frac{-N_o x}{\rho} = -xD\left.\frac{dc}{dy}\right|_o \tag{12}$$

Assumed Profiles

If the velocity and concentration profiles are self-preserving then by suitable scaling each profile can be reduced to a single dimensionless expression which is independent of the radial distance. The following dimensionless variables are defined

$$\frac{c - c_\infty}{c_o - c_\infty} = \phi(\eta_c) \tag{13}$$

$$\frac{u}{U(x)} = \zeta(\eta_m) \tag{14}$$

where

$$\eta_c = y/\delta_c(x) \tag{15}$$

$$\eta_m = y/\delta_m(x) \tag{16}$$

$\delta_c(x)$ and $\delta_m(x)$ are arbitrary measures of the concentration and momentum boundary-layer thicknesses, respectively. $U(x)$ is an arbitrary velocity, characteristic of the velocity profile at any radial distance.

Velocity Profile. Glauert showed that the dimensionless velocity profiles in the plane and radial wall jets are identical. Schwarz and Caswell tried several expressions for the velocity profile and found that the wall shear as calculated from their approximate solution agreed to within 2.7% with Glauert's exact expression when $\zeta(\eta_m)$ was taken as

$$\zeta(\eta_m) = \eta_m(1 - \eta_m^2) \tag{17}$$

This expression will be adopted in the following development.

Concentration Profile. The concentration profile can be approximated by a third-order polynomial which leads to the expression

$$\phi(\eta_c) = 1 - \frac{3}{2}\eta_c + \frac{1}{2}\eta_c^3 \tag{18}$$

Solution of the Momentum Integral Equation

When variables (14) and (16) are introduced, Equations (10) and (11) reduce to

$$\frac{\delta_m(x)}{U(x)}\frac{d}{dx}\left[xU^2(x)\,\delta_m(x)\int_o^\infty \zeta^2(\eta_m)\, d\eta_m\right] = -x\zeta'(0)\nu \tag{19}$$

and

$$F = x^2U^3(x)\,\delta_m^2(x)\left[\int_o^\infty \zeta(\eta_m)\int_o^\infty \zeta^2(\eta_m)\, d\eta_m \cdot d\eta_m\right] \tag{20}$$

If the form of the velocity profile $\zeta(\eta_m)$ is assumed then these equations can be solved for $U(x)$ and $\delta_m(x)$. With the approximate expression (17), the integrals in Equations (19) and (20) may be evaluated

$$I_1 = \int_o^\infty \zeta^2(\eta_m)\, d\eta_m = 8/105 \tag{21}$$

$$I_2 = \int_o^\infty \zeta(\eta_m)\int_o^\infty \zeta^2(\eta_m)\, d\eta_m \cdot d\eta_m = 0.00981 \tag{22}$$

Also

$$[+\zeta'(0)] = 1 \tag{23}$$

When $\delta_m(x)$ is eliminated from Equations (19) and (20) one obtains

$$\frac{1}{2}\left[\frac{F}{I_2}\right]U^{-3}(x)\frac{dU(x)}{dx} = \frac{-\zeta'(0)\nu x^2}{I_1} \tag{24}$$

which upon integration gives

$$U(x) = \left[\frac{4}{3}\frac{\zeta'(0)\nu}{I_1}\right]^{-1/2} x^{-3/2}\left[\frac{F}{I_2}\right]^{1/2} \tag{25}$$

Similarly

$$\delta_m(x) = \left[\frac{4}{3}\frac{\zeta'(0)\nu}{I_1}\right]^{3/4} x^{5/4}\left[\frac{F}{I_2}\right]^{-1/4} \tag{26}$$

Solution of the Mass Integral Equation

When variables (13) and (15) are introduced, Equation (12) becomes

$$\delta_c(x)\frac{d}{dx}\left[xU(x)\,\delta_c(x)\int_o^\infty \zeta(\eta_m)\,\phi(\eta_c)\,d\eta_c\right] = -xD\phi'(0) \quad (27)$$

The integral in Equation (27) involves both the velocity and the concentration profiles. Its numerical value will therefore depend on the relative rates of momentum and mass diffusivity, that is, the Schmidt number. However, if the profiles are self-preserving and have a common origin, then

$$\frac{\delta_c(x)}{\delta_m(x)} = \text{a constant} = \Delta \quad (28)$$

With this expression and Equation (28), the integral in Equation (27) can be expressed as

$$\int_o^\infty \zeta(\eta_m)\,\phi(\eta_c)\,d\eta_c = \left[\frac{\Delta}{10} - \frac{3\Delta^3}{140}\right] \quad (29)$$

Also

$$[-\phi'(0)] = 3/2 \quad (30)$$

When Equations (25), (26), (28), and (29) are introduced, Equation (27) becomes

$$\Delta x^{5/4}\frac{d}{dx}\left\{x^{3/4}\Delta\left[\frac{\Delta}{10} - \frac{3\Delta^3}{140}\right]\right\} = +\frac{3}{4}\frac{DI_1x[-\phi'(0)]}{\nu\zeta'(0)} \quad (31)$$

If, for the system, the rate of momentum diffusivity is the same as the rate of mass diffusivity, that is, the Schmidt number is 1.0, then Δ is of the order of one. If N_{Sc} is of the order of 1,000, then $\Delta << 1.0$ and $3\Delta^3/140$ may be neglected with respect to $\Delta/10$ enabling Δ to be solved for explicitly in Equation (31). The development will therefore be restricted to Schmidt numbers greater than unity.

When Equation (31) is integrated and Δ is regarded as a constant, one obtains

$$\Delta = \left(\frac{8}{7}\right)^{1/3} N_{Sc}^{-1/3} \quad (32)$$

If a circular area of the wall, of radius ξ, is not coated with solute, (Figure 1), it is apparent that the origins of the concentration and momentum boundary layers are not coincident and Δ is therefore no longer a constant but a function of x. Integration of Equation (31) from ξ to x gives

$$\Delta = \left(\frac{8}{7}\right)^{1/3} N_{Sc}^{-1/3}\left[1 - \left(\frac{\xi}{x}\right)^{9/8}\right]^{1/3} \quad (33)$$

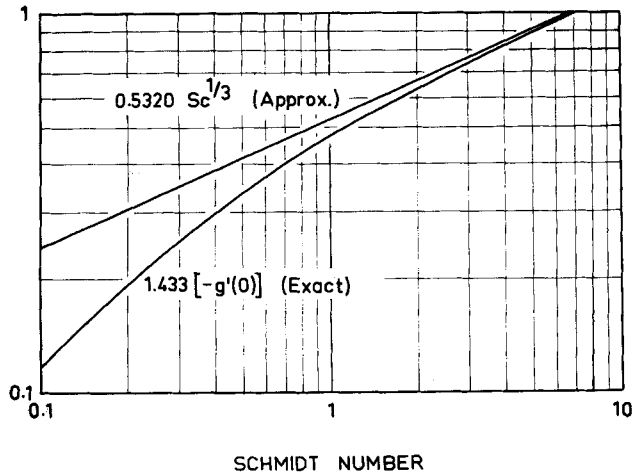

Fig. 2. Comparison of the exact and approximate solutions for low Schmidt numbers.

Mass Transfer Coefficient

When variables are transformed with Equations (13), (15), and (28), the mass transfer coefficient, k, as defined by Equation (8), becomes

$$k = \frac{D}{\Delta\delta_m(x)}[-\phi'(0)] \quad (34)$$

Substituting expressions (26) and (32) for $\delta_m(x)$ and Δ and putting in the numerical value of $[-\phi'(0)]$ gives

$$k = 0.5320\,D\,N_{Sc}^{1/3}\left[\frac{F}{\nu^3}\right]^{1/4} x^{-5/4} \quad (35)$$

If $\xi \neq 0$,

$$k = 0.5320\,D\,N_{Sc}^{1/3}\left[\frac{F}{\nu^3}\right]^{1/4} x^{-5/4}\left[1 - \left(\frac{\xi}{x}\right)^{9/8}\right]^{-1/3} \quad (36)$$

DISCUSSION OF THEORY

Comparison of the Exact and Approximate Solutions

For the special case of $l = 0$ and $\xi = 0$, a comparison between the exact and approximate solutions, Equations (9) and (36) can be drawn.

For $N_{Sc} = 1{,}000$, ignoring for the moment those terms common to both expressions, the exact solution gives

$$1.433\,[-g'(0)] = 5.349 \quad (37)$$

and the approximate solution gives

$$0.5320\,Sc^{1/3} = 5.320 \quad (38)$$

This agreement is good, the deviation being only 0.54%. This error could arise only from the assumption that $3\Delta^3/140 << \Delta/10$, leading to Equation (32), or the deviation of the assumed velocity and concentration profiles from the exact profiles.

Figure 2 is a plot of Equations (37) and (38) vs. the Schmidt number. It is apparent that the exact and approximate solutions converge rapidly for Schmidt numbers above one.

Eliminating the Gamma Functions

A way of removing the awkward gamma functions involved in $[-g'(0)]$ in the exact solution, Equation (9), is to expand the gamma functions in terms of Stirling's asymptotic series (*4*). It can be shown that for large values of the Schmidt number, Equation (7) reduces to

$$[-g'(0)] = 0.3733\,N_{Sc}^{1/3} \quad (39)$$

When this is put into the left-hand side of Equation (37) and $N_{Sc} = 1{,}000$, one obtains

$$0.5349\,N_{Sc}^{1/3} = 5.349 \quad (40)$$

which shows agreement to better than 0.02% with the exact expression.

Practical Application of the Theory

The experimental radial wall jet is in this case initiated by a round free jet impinging normally on a flat plate. Equations (9) and (36) contain two parameters, F and l, whose values will depend on the initiating jet, so coupling the mass transfer in the wall jet and flow conditions in the nozzle. An estimate of the value of these two parameters can be made as follows.

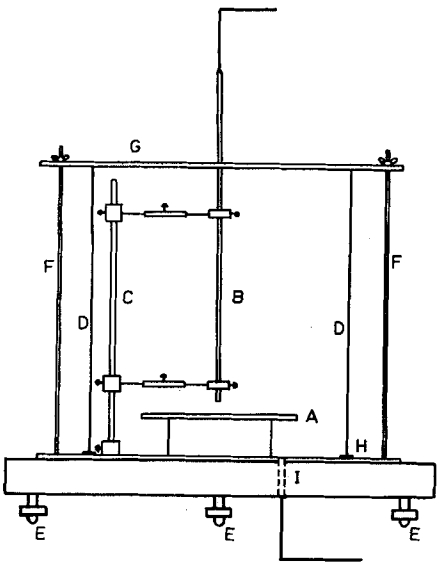

Fig. 3. Apparatus. A-surface plate, B-nozzle, C-nozzle support, D-plexiglass cylinder, E-leveling screws, F-tension rods, G-top plate, H-annular gasket, I-inlet/outlet.

Glauert suggested that the constancy of F, Equation (5), does not depend on the velocity profile having attained its final form. Assuming that the momentum of the jet is not affected by its being deflected by the plate, F may be estimated in the nozzle.

Evaluating Equation (5) for flow in the nozzle

$$F_e = \frac{\bar{u}^3 d^4}{128} \tag{41}$$

It has been suggested (2) that l be estimated by equating the volumetric flux in the wall jet at $x = 0$ to that in the nozzle giving

$$\frac{l_e}{d} = 0.1327\, N_{Re}^{1/3} \tag{42}$$

where N_{Re} is the Reynolds number in the nozzle.

A Practical Equation. From the results of the preceding sections a final equation can be deduced to relate mass transfer in the wall jet to flow in the nozzle.

When Equations (9) and (39) are combined, F is replaced by Equation (41), and the ξ factor from Equation (36) is introduced, one obtains

$$k = 0.1590\, D\, N_{Sc}^{1/3}\, N_{Re}^{3/4} \left[\frac{d}{x^5}\right]^{1/4} \left[1+\left(\frac{l}{x}\right)^3\right]^{-3/4} \left[1-\left(\frac{\xi}{x}\right)^{9/8}\right]^{-1/3} \tag{43}$$

Owing to the incorporation of the approximate expression (39) and the assumption involved in Equation (32), the validity of this equation is restricted to Schmidt numbers greater than one. For $l = 0$ and $\xi = 0$, the deviation from the exact expression for $N_{Sc} = 1.0$ is 12%. For Schmidt numbers of 2.0, 10, 100 and 1,000, the deviations are 5.8%, 1.05%, 0.08%, and 0.02%, respectively. At a Schmidt number of 0.1, the error exceeds 100%. Equation (43) is therefore a reasonable approximation to the exact solution for gaseous systems with Schmidt numbers greater than 2.0 as well.

EXPERIMENTAL

The following series of runs were made:

1. Data were obtained for comparison with theory in the Reynolds number range of 300 to 5,000 using three nozzle diameters. Data at radial distances less than 1 cm. were not taken.
2. These data were extended to radial distances less than 1 cm. by making detailed measurements in the region of the stagnation point.
3. Point mass transfer coefficients were measured with an uncoated starting length ξ.
4. Data for a range of Schmidt numbers of 970 to 4,400 were obtained at a Reynolds number of 1,000.

The coating materials used were acetanilide and benzoic acid. The Schmidt number was varied by the addition of small amounts of carboxymethylcellulose (CMC) which has been shown by experiment to increase the viscosity of water appreciably without significantly affecting the density or the solute diffusivity. If the concentration of CMC is small, the departure from Newtonian behavior can be neglected. With this method a comparatively large range of Schmidt numbers was attained which was not possible by merely changing the solute material. Since small quantities of electrolytes reduce the viscosity of CMC solutions considerably, only acetanilide was used in conjunction with CMC.

Apparatus

The apparatus is shown in Figure 3. The nozzle (B) is held over the center of the plate (A) in a normal position by the nozzle arm (C) which permits adjustment of the nozzle-to-plate distance and the vertical position. Three nozzles, made from stainless steel surgical tubing, of diameters 0.265, 0.467, and 0.625 cm. were used. The plate was 6.5 in. square and was made from 3/16-in. steel plate. The measuring instrument used was a thickness gauge which is graduated in 10,000ths of an inch (0.1 mils), each revolution of the pointer being one 100th of an inch. The instrument had a maximum range of 0.125 in. The gauge was supported above the plate by a bridge which spanned the plate and rested with its three knife edges on the plate. By means of graduations scribed on the edges of the plate, the position of the instrument probe with respect to the center of the plate could be set accurately. Surrounding the plate and nozzle support was a 12 × 13D × ¼ in. removable plexiglass cylinder held to a watertight seal with the base plate by means of a rubber gasket (D). Provision was made for the rapid filling and draining of the chamber so formed through a tube located under the plate. Distilled water from an overhead constant level tank was used. For runs with CMC solution a separate storage tank was used, and the solution was continuously circulated to the overhead tank. During the run the liquid level was maintained in the chamber by means of an overflow device.

Coating Procedure

The coating material was applied to the plate in the molten state and confined until it had solidified. A coating thickness of the order of 0.03 in. was found to be suitable for a run. The surface coating was wetted and scraped with a sharp-edged tool and finally wiped down with hot water. This gave a very smooth coating of fairly uniform thickness.

Surface Profile Measurements

As a general procedure the gauge was traversed across the plate in two directions in steps of 0.5 cm. giving four point readings equidistant from the center of the plate and $\pi/2$ radians apart. In some runs, the area of the coating nearest to the stagnation point was of prime interest and readings at smaller intervals of distance were therefore taken in this region. When required, an uncoated starting length, ξ, was introduced by covering the center of the coating with a circular disk of polyethylene film which prevented the boundary layer from contacting the solute until it had passed beyond the edge of the disk. Silicone grease was used to hold the film in position.

Making a Run

A coating was applied and a profile taken. The nozzle was then lined up accurately over the center of the plate and in a normal position using a plumb line. A nozzle-to-plate distance of ¼ in. was used for all runs. With the plexiglass cylinder in place, the chamber was filled with liquid from the overhead

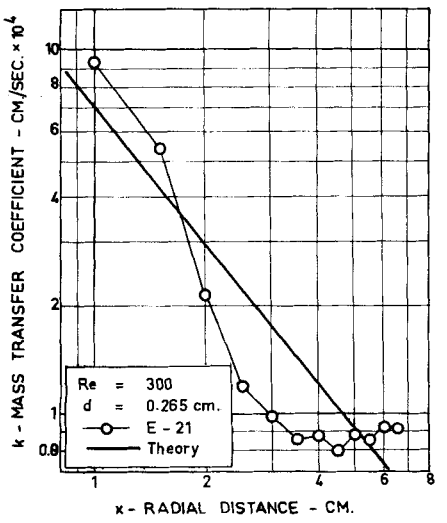

Fig. 4. Comparison of experimental and theoretical mass transfer coeffiicents.

tank. During the run the liquid flow rate was measured by means of a rotameter. The run was terminated when the center of the plate became bare. A second surface profile measurement was made after the run giving the total decrease in coating thickness. These measurements were corrected for the mass transfer which took place during the filling and draining periods. A blank run of zero run time showed that some 12% of the total mass transfer near the edge of the plate took place during these periods, while at the center, the blank was of the order of 1%.

Calculation of Point Mass Transfer Coefficients

It is easily shown that if the bulk concentration is zero, as for the present case, then

$$k = \frac{\Delta t\ 2.54\ \rho_s}{1000\ \theta\ c_s}$$

From profile measurements at each radial distance, four values of the point thickness decrease were obtained. A random variation of the order of 0.3 mils was observed between these four measurements. The thickness measurements are estimated to be accurate to 0.1 mils. These larger deviations could be owing to surface irregularities which develop during the run. The relevant data for acetanilide and benzoic acid are given in the appendix. The experimental error in the calculated value of the mass transfer coefficient is estimated to vary from 3% at the center of the coating to 12% at the edges where the thickness decrease during the run is comparatively small.

RESULTS AND DISCUSSION

Variation of the Reynolds Number

The results obtained are shown in Figures 4 to 7 where the experimental mass transfer coefficient has been plotted vs. radial distance. The theoretical line, Equation (43) has also been plotted for comparison. For these runs the starting length is zero. The parameter l as estimated from Equation (42) has little effect for $x/d > 2.5$ and has been neglected in the theoretical plot for the smallest nozzle.

Unexpected results were obtained for $N_{Re} < 1{,}000$ as is seen in Figures 4 and 5. The deviation from theory is most severe at $N_{Re} = 300$ while at $N_{Re} = 700$ it was found to be comparatively slight. It was possible to observe the flow pattern by means of a dye streak introduced with a very fine capillary. At $N_{Re} = 300$, it was found that at a radial distance of approximately 1.5 cm., boundary-layer separation occurred with the formation of a toroidal vortex centered around the nozzle. A quantity of dye was also introduced on to the plate beyond the separation point and it was found that outside the vortex, the fluid adjacent to the plate was virtually stagnant with no evidence of a counter vortex.

A close correlation was evident between the experimental data and visual observation. The point of boundary-layer separation corresponds to the point where the data fall below the predicted values. Outside the vortex, $x > 3$ cm. mass transfer would be mainly by molecular diffusion leading to the flat section of the curve for $x > 3$ cm. in Figure 4. A similar correlation was found for $N_{Re} = 400$. The vortex was larger than that which forms at $N_{Re} = 300$ and not as stable. It could easily be destroyed by slight disturbances in the fluid surroundings but reestablished itself when left undisturbed. At still higher Reynolds numbers, 500 and 700, no vortex was formed although boundary-layer separation was still observed. The fluid adjacent to the plate was no longer stagnant after the point of separation and the mass transfer rate was therefore higher in this region than at lower Reynolds numbers. At $N_{Re} = 1{,}000$, no boundary-layer separation was observed. Dye streak photographs of the boundary-layer behavior at low Reynolds numbers are to be found in reference 6. Glauert (3) accounts for this observed separation in terms of entrainment in the wall jet of fluid from outside the boundary layer.

For $N_{Re} = 1{,}000$ to 3,000, the agreement between the experimental data and theory is good. A typical set of data is shown in Figure 6; other results are shown in reference 6. The increased scatter at the larger values of x is owing to the relatively small thickness decrease measurement and hence the larger relative error near the edge of the plate. The reproducibility of these data is good as is shown in Figure 6 where duplicate runs have been plotted.

At $N_{Re} = 5{,}000$ observations showed the boundary layer to be no longer laminar, and higher transfer rates in Figure 7 were therefore to be expected.

Mass Transfer Near the Stagnation Point

The wall jet is initiated by a round free jet and the wall jet theory is therefore not valid in the region of the stagnation point. As has been shown, the effect of the estimated value of l is small for $x/d > 2.5$. To investigate the effect of l nearer to the impingement point, data for $x/d < 2.5$ were taken at $N_{Re} = 1{,}000$ with the three nozzle diameters. Figure 8 shows these data for the largest nozzle along with the data for $x > 1$ cm. The two sets of data were taken separately and are seen to match up well in the region of overlap. Also shown are the theoretical curves with $l = l_e$ and $l = 0$. In all these runs it would appear that the estimated value of l is far too large if indeed the theory has any significance at all so close to the nozzle axis.

Effect of an Uncoated Starting Length

The approximate solution of the mass balance equation using assumed velocity and concentration profiles led to the ξ term in Equation (43). Mass transfer coefficients at $N_{Re} = 2{,}000$ were measured with the smallest nozzle diameter. Starting lengths of 1.53 cm. and 3.18 cm. were used. These data are plotted in Figures 9 and 10. Also shown are the corresponding data for $\xi = 0$. As predicted by theory the effect of ξ is to increase the value of k at all radial distances. Agreement with theory is good.

The Exterior Flux of Momentum Flux

It has been shown that on the assumption that the momentum of the impinging jet remains unchanged on deflection by the plate, the value of F can be conveniently calculated in the nozzle. Using this estimated value of F, $N_{Sh}(x/d)^{1/4}$ should vary as $N_{Re}^{3/4}$. Figure 11 shows such

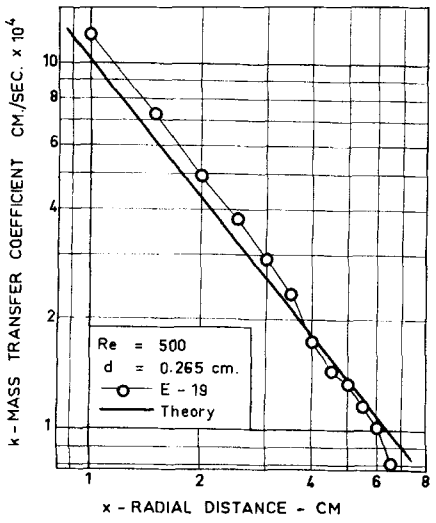

Fig. 5. Comparison of experimental and theoretical mass transfer coefficients.

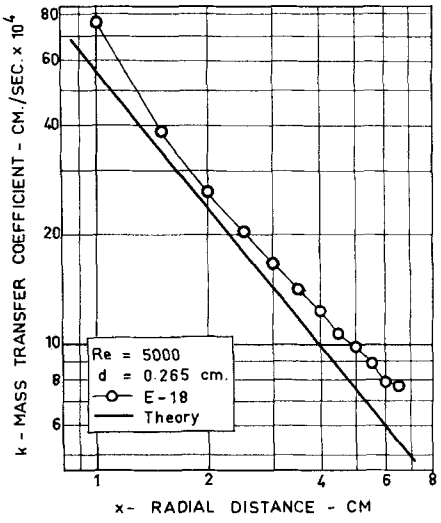

Fig. 7. Comparison of experimental and theoretical mass transfer coefficients, N_{Re} = 5,000.

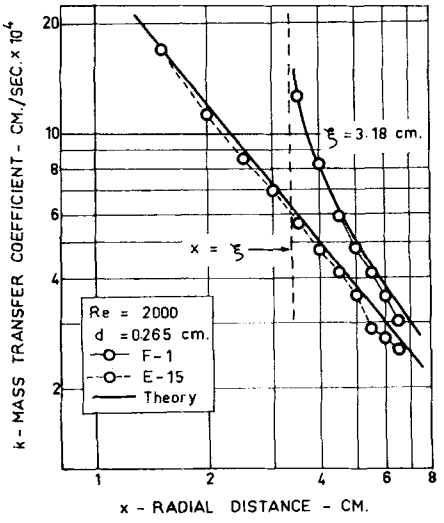

Fig. 9. The effect of an uncoated starting length on the mass transfer coefficient. Comparison with theory.

a plot of the experimental data. The average standard deviation in the values of $N_{Sh}(x/d)^{1/4}$ for each Reynolds number is ± 16.2. For Reynolds numbers less than 1,000, only those values of k before the point of separation were considered. The point for N_{Re} = 5,000 is high, as was expected, owing to the onset of turbulence and is plotted merely for comparison.

For N_{Re} = 1,000 to 3,000 the data agree well with the theory. This shows that the estimated value of the exterior flux of momentum flux in the nozzle is a good approximation to F in the wall jet. At Reynolds numbers less than 1,000 the high values of $N_{Sh}(x/d)^{1/4}$ are understandable as, with the formation of a vortex, some of the fluid and with it momentum is fed back into the boundary layer. This leads to an increase in the value of F in the wall jet and so increases the value of the mass transfer coefficient. The observed values of k before the point of separation were some 30% high.

Variation of Schmidt Number

Figure 12 shows the variation of $N_{Sh}(x/d)^{1/4}$ in the range of Schmidt numbers from 970 to 4,400 for N_{Re} = 1,000. The data in this plot show a greater scatter than was expected on the basis of the other results. Since CMC solutions are very difficult to filter, this scatter could be owing to inaccuracies in the viscosity determinations caused by insoluble particles in the CMC. In addition the flow of CMC solution through the needle valve fluctuated and required constant adjustment. Dye streak observations showed that these sudden changes in the flow rate caused short periods of separation in the form of small transient vortices which would lead to lower transfer coefficients. With pure water the flow remained perfectly steady.

SUMMARY AND CONCLUSIONS

An exact solution of the mass conservation boundary-layer equation has been obtained, as well as an approximate solution of the integral mass balance equation, with assumed forms of the velocity and concentration profiles. The exact solution involved gamma functions of the Schmidt number which are tedious to evaluate for Schmidt numbers much greater than one.

By expanding the gamma functions an approximate expression for the point mass transfer coefficient was obtained and compared with the corresponding exact form.

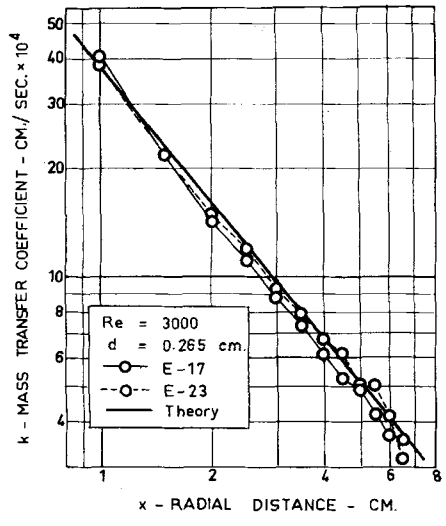

Fig. 6. Comparison of experimental and theoretical mass transfer coefficients, N_{Re} = 3,000.

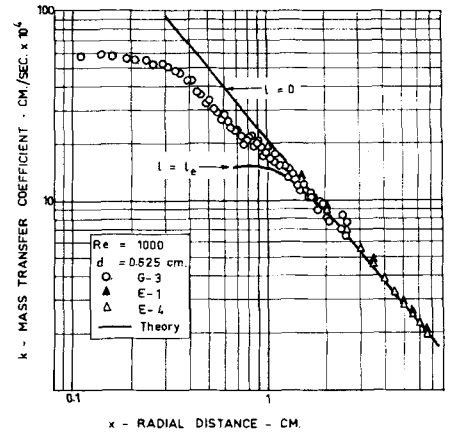

Fig. 8. Comparison of experimental and theoretical mass transfer coefficients near the impingement point. Large nozzle.

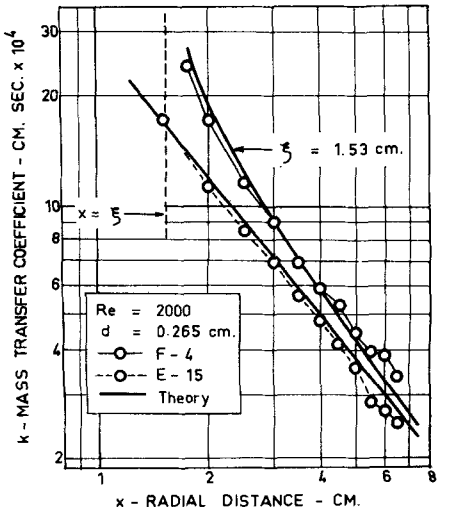

Fig. 10. The effect of an uncoated starting length on the mass transfer coefficient. Comparison with theory.

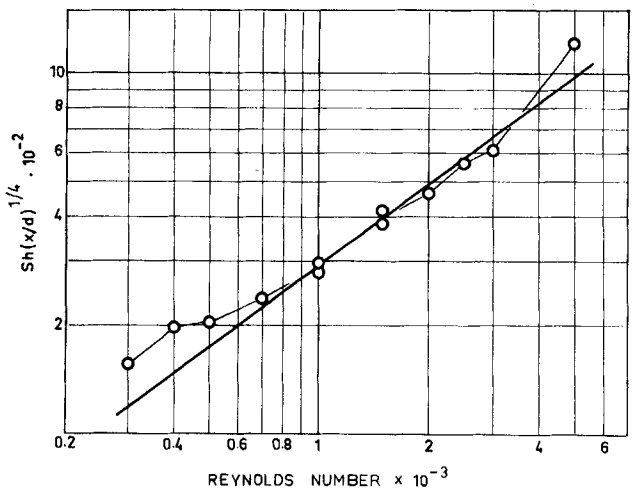

Fig. 11. Variation of the Sherwood number with Reynolds number. Comparison with theory. $N_{Sc} = 1{,}090$.

For Schmidt numbers of the order of 1,000 the error involved in the approximation was less than 0.02%. For lower Schmidt numbers, the deviations were somewhat larger, namely, 1.05% at $N_{Sc} = 10$ and 12% at $Sc = 1.0$.

Point mass transfer data were obtained for $N_{Re} =$ 1,000 to 3,000, $x/d = 2.5$ to 25, $N_{Sc} = 970$ to 4,400, and with and without a starting length ξ. Agreement with theory was good. At lower Reynolds numbers boundary-layer separation was observed which led to vortex formation for $N_{Re} < 500$. At $N_{Re} = 5{,}000$, the wall jet, for $x/d < 25$, was no longer laminar.

It was concluded that:

Equation (43) can be used to predict point mass transfer coefficients in good agreement with experimental data in the range of variables given.

The velocity and concentration profiles, at least near the wall, are self-preserving.

The exterior flux of momentum flux in the wall jet can be satisfactorily estimated in the nozzle of the impinging jet.

The estimated value of the length parameter l did not account for data at $x/d < 2.5$.

NOTATION

c = concentration of solute, g./cc.
c_s = solubility of solute, g./cc.
d = nozzle diameter, cm.
D = solute diffusivity, sq. cm./sec.
F = exterior flux of momentum flux, cm.^{7}/sec.^{3}
k = point mass transfer coefficient, cm./sec.
l = length parameter (Glauert), cm.

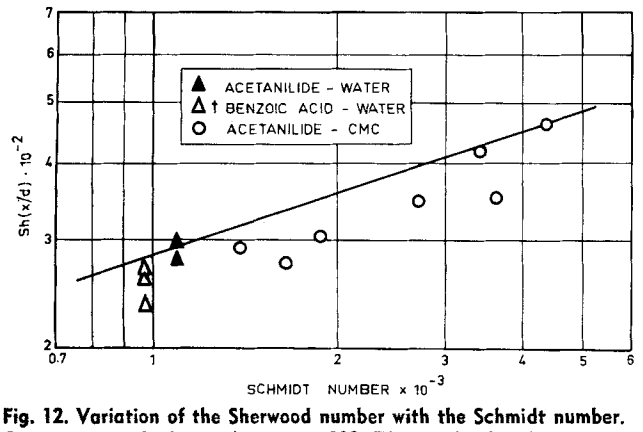

Fig. 12. Variation of the Sherwood number with the Schmidt number. Comparison with theory. $N_{Re} = 1{,}000$. The results for the benzoic acid-water system are taken from a B.A.Sc. thesis by E. G. Benko at the University of Toronto, Toronto, Ontario, Canada (1962).

N = solute mass flux normal to the wall, g./sq. cm. sec.
$U(x)$ = velocity characteristic of boundary layer, cm./sec.
u = radial component of velocity along wall, cm./sec.
$\bar{u}$ = average fluid velocity in nozzle, cm./sec.
v = component of velocity normal to wall, cm./sec.
x = radial distance along wall, cm.
y = distance normal to wall, cm.

Greek Letters

δ = boundary-layer thickness, cm.
δ_c = concentration boundary-layer thickness, cm.
δ_m = boundary-layer thickness, cm.
Δt = thickness decrease of coating, mils.
θ = run time, sec.
ν = kinematic viscosity, sq. cm./sec.
ξ = uncoated starting length, cm.
ρ = fluid density, gm./cc.
ρ_s = coating density, gm./cc.
τ = fluid shear stress, dynes/sq. cm.

Dimensionless Quantities

N_{Re} = Reynolds number in nozzle, $= \bar{u}d/\nu$
N_{Sc} = Schmidt number, $= \mu/\rho D$
N_{Sh} = Sherwood number, $= kx/D$
$g(\eta)$ = concentration profile (exact)
$\zeta(\eta_m)$ = velocity profile (approximate)
$\phi(\eta_c)$ = concentration profile (approximate)
$\Gamma(n)$ = gamma function of n
Δ = ratio $\delta_c(x)/\delta_m(x)$
η = distance from wall, $= y/\delta$
η_c = distance from wall, $= y/\delta_c$
η_m = distance from wall, $= y/\delta_m$

Subscripts

e = estimated value
o = wall condition

Superscript

$'$ = differentiation with respect to the distance parameter

LITERATURE CITED

1. Glauert, M. B., *J. Fluid Mech.*, **1**, 625 (1956).
2. Schwarz, William H., and Bruce Caswell, Paper presented at the A.I.Ch.E. and C.I.C. Joint Chemical Engineering Conference, Cleveland, Ohio (May, 1961).
3. Glauert, M. B., "Boundary-layer Research," ed. H. Gortler, p. 72, Springer-Verlag (1958).
4. Davies, H. T., ed., "Tables of Higher Mathematical Functions," Vol. 1, Principia, Bloomington, Indiana, (1933).
5. Steel, L. R., and C. J. Geankoplis, *A.I.Ch.E. Journal*, **5**, 178 (1959).
6. Scholtz, M. T., M.A.Sc. thesis, University of Toronto, Toronto, Ontario, Canada (1961).

Manuscript received September 14, 1962; revision received February 11, 1963; paper accepted February 13, 1963. Paper presented at A.I.Ch.E. New Orleans meeting.

APPENDIX

Properties of Benzoic Acid and Acetanilide

	ρ_s, g./cc., 25°C.	Solubility g./100 ml. 24°C.	25°C.	26°C.	$D_{25°} \times 10^5$, sq. cm./sec.	$N_{Sc25°}$
Acetanilide*	1.124	0.609	0.621	0.640	0.820	1090
Benzoic acid	1.202	—	0.338†	—	0.935†	970†

* The solubility data for acetanilide were determined from supersaturated solution and the diffusivity was found with a stirred diaphragm cell. Acetanilide was conveniently determined by hydrolysis in boiling 5*N* hydrochloric acid followed by bromination. Three bromine atoms substitute rapidly and quantitatively on the aniline hydrochloride formed by hydrolysis.

† Taken from reference (5).